Article

Characterization of Thin AlN/Ag/AlN-Reflector Stacks on Glass Substrates for MEMS Applications

Christian Behl [1,*], Regine Behlert [1,†], Jan Seiler [1,2], Christian Helke [1,2] , Alexey Shaporin [1] and Karla Hiller [1,2]

1   Fraunhofer Institute for Electronic Nano Systems (ENAS), Technologie-Campus 3, 09126 Chemnitz, Germany; jan.seiler@enas.fraunhofer.de (J.S.); christian.helke@enas.fraunhofer.de (C.H.); karla.hiller@enas.fraunhofer.de (K.H.)
2   Center for Microtechnologies (ZfM), TU Chemnitz, Reichenhainer Str. 70, 09126 Chemnitz, Germany
*   Correspondence: christian.behl@enas.fraunhofer.de; Tel.: +49-45001-610
†   Current address: Carl Zeiss, Carl-Zeiss-Promenade 10, 07745 Jena, Germany.

Abstract: Thin metal layers such as silver (Ag) are being utilized for various optical and plasmonic applications as well as for electrical purposes, e.g., as transparent electrodes in display devices or solar cells. This paper focuses on optical MEMS applications such as the Fabry–Pérot interferometer (FPI). Within such filters, reflector materials such as distributed Bragg reflectors (DBRs) or subwavelength gratings (SWGs) have been widely used so far, whereas metallic thin films (MTFs) were limited in application due to their comparatively higher absorption. In this paper, thin sputtered Ag layers with thicknesses of 20, 40 and 60 nm on glass substrates have been investigated, and it is shown that the absorption is very low in the visible spectral range (VIS) and increases only in near-infrared (NIR) with increasing wavelength. Thus, we consider Ag-thin layers to be an interesting reflector material at least for the VIS range, which can be easily fabricated and integrated. However, Ag is not inert and stable when exposed to the atmosphere. Hence, it needs a passivation material. For this purpose, AlN has been chosen in this contribution, which can be deposited by sputtering as well. In this contribution, we have chosen thin AlN layers for this purpose, which can also be deposited by sputtering. Thus, various AlN/Ag/AlN-reflector stacks were created and patterned by lift-off technology preferably. The fabricated reflectors were characterized with respect to adhesion, stress, cohesion, homogeneity, and most importantly, their optical properties. It was found that the thickness of the AlN can be used to adjust the reflectance–transmittance ratio in the VIS range, and influences the adsorption in the NIR range as well. Based on the measured values of the reflectors with 40 nm Ag, an exemplary transmission filter characteristics has been predicted for a wavelength range from 400 to 800 nm. Both the maximum transmittance and the full width at half maximum (*FWHM*) can be tuned by variation of the AlN thickness from 20 to 60 nm.

Keywords: metallic thin film; Fabry–Pérot interferometer; visible spectral range; near-infrared; subwavelength gratings; distributed Bragg reflector

1. Introduction

Originally optical spectrometers have been large and very cost intensive devices. In the past couple of years, handheld instruments have been designed to make them portable at lower production costs by the use of a micro machined spectrometer, e.g., MEMS FPI [1–5].

Basically, the principle of a MEMS FPI can be described with two-plane, parallel, and semi-transparent reflectors with a gap d, as shown in Figure 1. The incident light I_0 can transmit through the semi-transparent mirror. For resonant wavelengths, it is reflected several times in the cavity and constructive interference will occur (see Equation (1)), with m being the order or the filter. Finally, the transmitted light intensity I_t is the output signal of the FPI, which is a periodic signal with respect to the spectrum. Furthermore, Figure 1 shows also the Free Spectral Range (*FSR*, described by Equation (2)), which is the distance

between two adjacent peaks, and the *FWHM*, described by Equation (3)), determining the bandwidth or resp. resolution of the filter. Both for the *FWHM* and the finesse of the filter (see Equation (4)), the reflectance *R* of the mirrors is most important and is typically targeted in a range of 70 to 97%. Furthermore, the maximum transmission is influenced by the absorption within the optical layers (see Equation (5)). Hence, for application in FPI, the choice of an appropriate reflector material with high and preferably adjustable reflectance over a wide wavelength range and low absorption is very important.

$$CWL = \frac{2d}{m} \tag{1}$$

$$FSR = \frac{2d}{m(m+1)} \tag{2}$$

$$FWHM = \lambda \frac{1-R}{\pi m \sqrt{R}} \tag{3}$$

$$F = \frac{4R}{(1-R)^2} \tag{4}$$

$$T_{max} = (1 - \frac{A}{1-R})^2 \tag{5}$$

The use of thin metals as opposed to previously implemented distributed Bragg reflectors [6–9] or subwavelength gratings [10,11] in optical gas sensors has been growing in recent decades due to the *MTF*'s advantages, such as an infinitely variable reflectivity of the mirror adjusted by the films' thickness, a comparatively less complex fabrication process, as well as an extraordinarily high reflectivity in VIS [12]. Previously held back by the higher absorption of metal materials, which DBR and SWG do not suffer from, MTFs are being used more often in optical sensor applications these days [13,14]. Silver is a very promising candidate for *MTF* and can be easily deposited by sputtering. However, Ag is not inert and stable when exposed to the atmosphere, and hence needs a passivation material. In this contribution, we have chosen thin AlN-layers for this purpose, which can be deposited by sputtering as well. Thus, AlN can be integrated relatively simply into the fabrication process, and has low absorption in VIS [15], and is transparent even for thicker layers. Several methods for patterning the optical layers stacks have been tested and will be described in Section 2. The fabricated reflectors have been characterized with respect to adhesion, stress, cohesion, homogeneity, and most importantly, their optical properties.
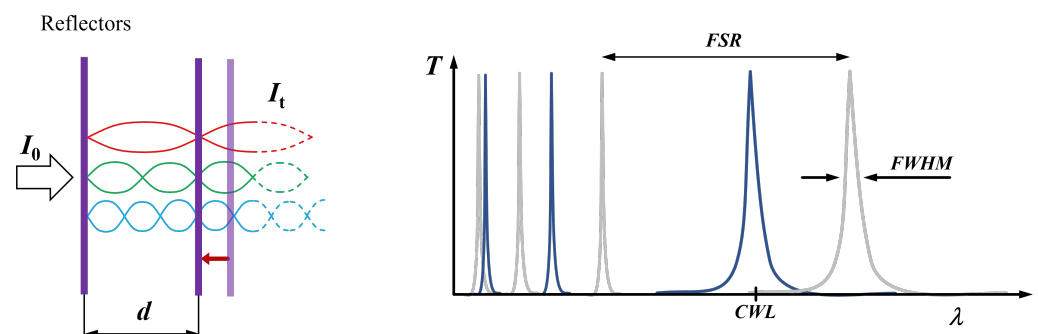

Figure 1. FPI principle: two parallel plane mirrors (**left**); peaks of transmission with important characteristics (**right**).

2. Fabrication and Inline Characterization of Reflectors

In terms of fabrication, three main methods have been carried out and compared to each other mainly with respect to the films' thickness, since varying the thickness of the Ag-thin film would drastically change the FPI's optical properties. Furthermore, with the step height $\bar{t}_{Ag}$ of Ag mirrors, which represents the films' thickness, the reflectance of the

same is adjustable. With that, the finesse [16] can be influenced and thus the resolution of the FPI.

The Ag-layers were sputtered via magnetron sputtering at the FHR1 MS150x4-AE D030 sputtering system and the AlN was deposited by a reactive sputter process at the FHR2 MS150x4-AE-B system.

2.1. Deposition of Pure Ag-Layers

To determine the homogeneity of the sputtered Ag-reflectors, the electrical four-point measurements was carried out at the Polytec 280 SI measurement system. The sheet resistance R_{sq} for all thicknesses exhibits $SD \leq 2\%$ or lower, which indicates that the thickness of the Ag-thin films is overall homogeneous.

In Table 1, not only the measured R_{sq} for various film thicknesses are listed, but also the specific conductivity κ, which has been calculated from these results. It can be observed that κ becomes smaller the thinner the film thickness is. For the bulk-material of Ag, the conductivity is about $\kappa = 66 \frac{\text{m}}{\Omega\text{mm}^2}$ and for a 20 nm thin film, only approximately $\kappa = 23 \frac{\text{m}}{\Omega\text{mm}^2}$. The cause for this size effect is the limited mean free path of the electrons, which more often collide with atoms or photons the thinner the *MTF* is.

Table 1. Target values of the thickness t with the measured sheet resistances R_{sq}, their standard deviation SD, as well as the calculated specific conductivity κ of the Ag-thin films.

t in nm	R in $\frac{\Omega}{sq}$	SD in %	κ in $\frac{\text{m}}{\Omega\text{mm}^2}$
20	2.16	2.01	23.15
40	0.89	2.08	28.09
60	0.54	1.98	30.86
100	0.29	1.74	34.48

Figure 2 shows 20, 40, 60 and 100 nm *MTF*'s on glass after wet etching. For 20 nm, it is evident that the surface does not cohere entirely. The reason for this observation is the Volmer–Weber growth of thin metal layers [17]. Therefore, small islands of liquid metal form first, followed by lateral growth, which then connects them with each other. For the 40 to 60 nm layers, the Ag is coherent for the entire surface, which is the basis for homogeneous film thickness and consistent reflectivity.
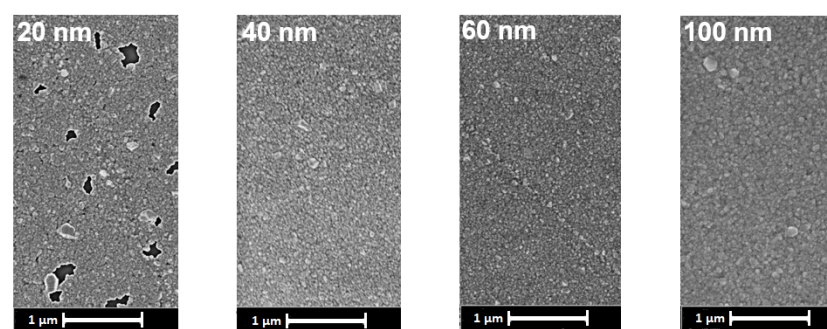

Figure 2. SEM top-view of Ag-thin films with different thicknesses.

To examine the cohesion of thin Ag-layers after deposition, the scanning electron microscope (SEM) Supra 60 from Zeiss was used.

In order to determine the residual stress (Equation (6)) of Ag on glass, the radii of curvature of the surface pre- and post-*MTF* deposition were recorded. Together with the Stoney equation [18], the residual stresses can be calculated.

$$\sigma = \frac{E_s t_s^2}{6(1 - \nu_s) t_{MTF}} \left(\frac{1}{R_0} - \frac{1}{R} \right)$$

(6)

Under the condition that the substrate thickness t_s is way bigger than the *MTF*'s thickness t_{MTF}, the residual stress σ of the thin film can be calculated. The modulus of elasticity E_s of the substrate, Poisson's ratio ν_s, and the radii of curvature R_0 before and R after the deposition are also needed.

The stress measurements as well as the step height measurements shown later, were carried out with a P-17 Stylus Profiler from KLA. Table 2 shows that the residual stress increases for decreasing film thickness. The reason for this behavior lies in size effects caused by an increasing ratio of surface to volume with the decreasing thickness of the layer [19]. The stress measurements showed that, for each film thickness, the average stress is positive, and thus, tensile stress results in a concave curvature of the wafer. Since the wafers themselves were already concave, they are still the same after thin-film deposition. The total difference from the lowest to the highest point of the glass wafers was about 45 μm for each. At 100 nm Ag, the stress is very low with 4 MPa. The influence that the Ag-thin film has on the curvature deflection is 0.6 μm, which also emerged from these measurements.

Table 2. Average stress of Ag-thin films with different thicknesses measured at P-17 profiler.

Target Value t in nm	Stress in MPa
20	62
40	43
60	12
100	4

In addition, the adhesion of the Ag-reflectors has been examined up to $11.8 \frac{N}{cm}$ by the tape peel test with pre-initiated cracks. Tape from Tesa was used with the adhesive strength of $3.6 \frac{N}{cm}$, $5 \frac{N}{cm}$ and $11.8 \frac{N}{cm}$, respectively. Whether structured with wet-, dry etching, or a lift-off process, the Ag has not been delaminated from glass substrate.

2.2. Structuring of Pure Ag-Reflectors and AlN/Ag/AlN-Reflector Stacks

For application in optical filters, circular patterns of the reflectors in groups of 2 or, respectively, 4 optical areas are required. All of the reflectors have a 2 mm diameter and were manufactured on 150 mm glass wafer substrates. An overview of the arrangement is given in Figure 3.
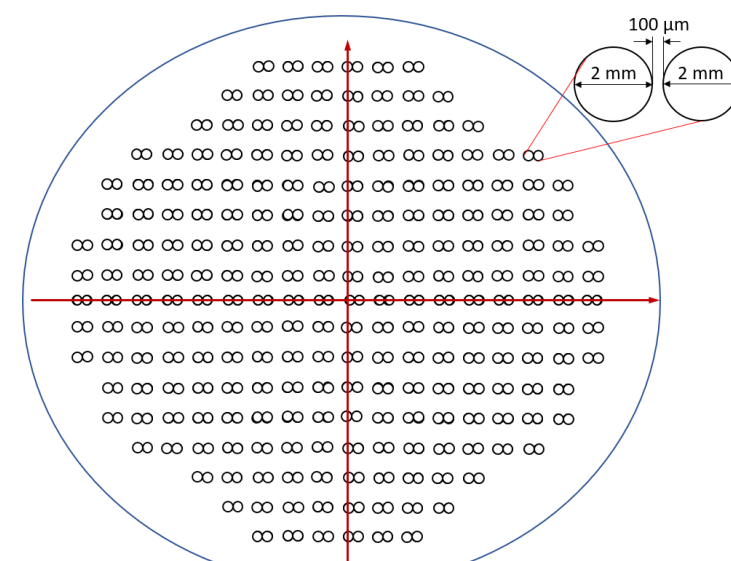

Figure 3. Wafer map illustrating the P-17 measuring spots on a 150 mm wafer and measurement direction for the vertical and horizontal sampling.

In the following, the Ag-reflectors structured by the three methods, wet etching, dry etching, and lift-off, are characterized with respect to the layer thickness and homogeneity. Whether it is an etching or lift-off process, structuring of course also includes the lithography in advance as well as the resist removal afterwards.

2.2.1. Wet Etch

The first method to be analyzed was the wet etching process. It is the most efficient way to structure thin metal materials in MEMS applications for larger quantities, since many wafers can be etched in one batch at the same time. The wet etching of these Ag-reflectors was performed with an $Fe(NO_3)_3$ solution.

For the characterization of the Ag-film thicknesses after wet etching, all the mean step heights $\bar{t}$ were sampled by the diamond needle of the P-17 profilometer. The red arrows in Figure 3 show the reflector pairs, at which the 35 measurements were carried out. On the top-right, a detailed view was given to demonstrate the dimensions. Regarding the profile, the needle starts on glass with the step up to the Ag-layer and then down to the glass wafer again.

Note that the layout is inverted for the wet etching process compared to the other structuring methods, so a larger coherent area of Ag remains on the wafers, to ensure other measurements, for example the sheet resistance, could be repeated later in the process chain again.

Later on, remaining photoresist was found with the Zygo NewView 7300 White Light Interferometer (WLI), that probably caused the diamond needle of the P-17 profilometer to deflect unintentionally, which resulted in a distortion of the step height measurements (see Table 3). In Figure 4, there is one example of the photoresist that covers the whole image like a curtain. The resist covers large areas on many of the Ag-reflectors fabricated by wet etching as it was not fully removed by the stripping process.
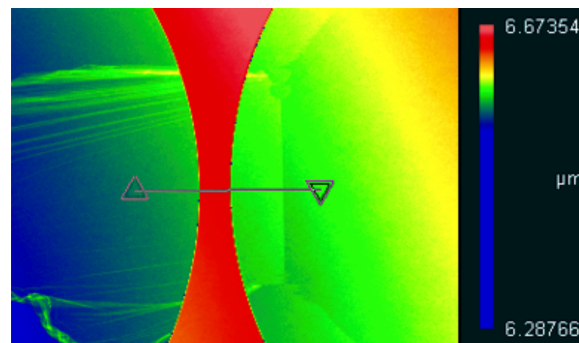

Figure 4. WLI measurement that shows remaining photoresist on Ag-reflectors.

Table 3. Fabricated reflectors with their respective thicknesses and a short evaluation.

	Material	Target Value t in nm	P-17 Step Height	FIB Film Thickness	Further Optimization
Wet etch	Ag	20	20 ± 13	-	Improve resist removal
	Ag	40	27 ± 19	54	Improve resist removal
	Ag	60	59 ± 15	77	Improve resist removal
	Ag	100	103 ± 13	115	Improve resist removal
Lift-off	Ag	20	52 ± 2	24	Optimize film thicknesses
	Ag	40	67 ± 2	67	Optimize film thicknesses
	Ag	40	72 ± 2	39	Optimize film thicknesses
	Ag	60	99 ± 3	74	Optimize film thicknesses
	Ag	100	133 ± 3	98	Optimize film thicknesses
	Ag/AlN/Ag	20/40/20	86 ± 1	-	Meets expectations
	Ag/AlN/Ag	20/40/20	89 ± 2	-	Meets expectations
	Ag/AlN/Ag	40/40/40	128 ± 3	-	Meets expectations
	Ag/AlN/Ag	60/40/60	172 ± 2	199	Meets expectations

2.2.2. Dry Etch

Another method for structuring Ag-reflectors is reactive ion etching (RIE). This is a chemical-physical etching process. The Ag was etched by BCl_3-ions with and without the addition of Ar-ions. These processes were performed at the FHR MS 200-2-AE system. After dry etching, the wafers were rinsed with DI-water, then spun in the centrifuge, and finally, the resist is stripped by an O_2/N_2 remote plasma whose radicals react with the photoresist. After these processes the reflectors were over etched, mostly in the center of the wafer, but also with outwards impact on the wafers' edge, as can be seen in Figure 5. The reason why this occurred might be that, after RIE, some BCl_3 remained on the wafer, which is known to react in contact with water to hydrochloric acid (HCl) and boric acid $(B(OH)_3)$. Thus, the acid could have continued to unintentionally etch further, until being removed by the centrifuge. This fabrication method could be improved in the future. For this work, we decided to focus on the lift-off process.
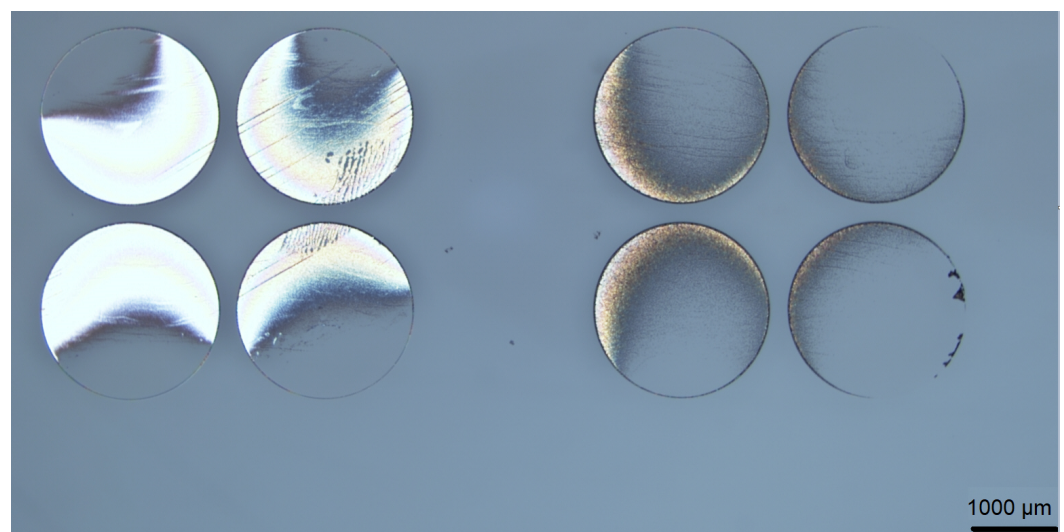

Figure 5. Microscope image of a 150 mm glass wafer with 40 nm Ag-reflectors after RIE with 30% Ar-ions.

2.2.3. Lift-Off

The third applied structuring method was via Lift-off process, which has been used for pure Ag as well as the AlN/Ag/AlN-reflector stacks. To briefly describe the flow: First, the resist ma-N 1420 was coated onto the wafer via spin-on, followed by exposure and development, so the structures of the reflectors are open. Then, the reflector material has been deposited by sputtering, and finally, the lift-off was realized, using DMSO remover. For this, the model SpinLift-off from AP&S was used. Figure 6 provides an overview of the reflectors fabricated on glass wafers. With this fabrication flow, there have not been any complications and the resulting Ag-reflectors are distributed the same as for the previous structuring methods, but without any of them being damaged.

A detailed look at one of the fabricated reflector pairs is given in Figure 7, while Figure 8 provides an overview of the measured film thickness after lift-off fabrication. In step height measurements, *SD* was much lower after lift-off process compared to wet etching. Also, the individual step measurement curves look much more uniform and consistent. However, the mean values do not correspond to the target values of the films thicknesses, which is most likely caused by the different growth of Ag-thin films on glass compared to other substrates like Si or SiO_2, for instance. For the target values of 20 nm and 40 nm, some cross-section measurements via focused ion beam (FIB) cut and subsequent SEM analysis were carried out, using the Auriga60 tool from Zeiss.
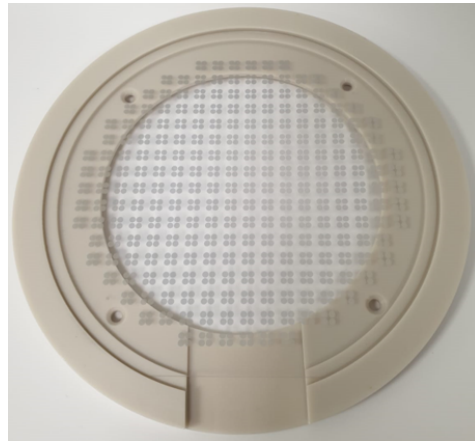
Figure 6. Image of 150 mm glass wafer with 40 nm Ag-reflectors after lift-off process.

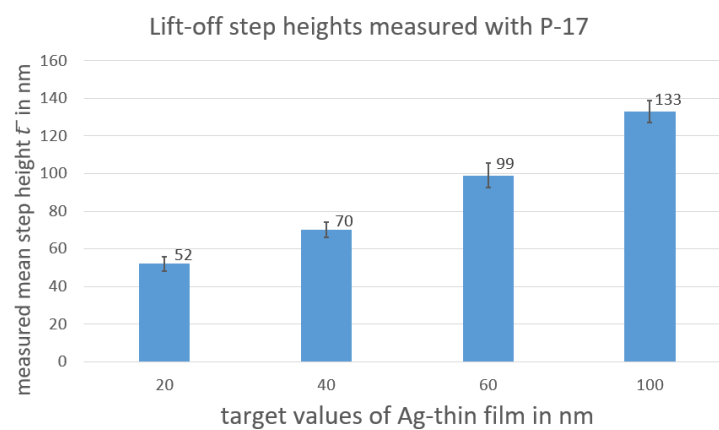**Figure 7.** Microscope image of a 40 nm Ag-reflector pair after lift-off.

Figure 8. Measured mean step height of Ag-reflectors structured by a lift-off process on a glass substrate.

In order to limit the impact of charge build-up of the glass substrate, a thin film of C has been deposited on the sample surface. On top of that, the Pt of a few nm thickness was applied to condition the FIB to make a perpendicular cut. The 20 nm Ag-reflectors were examined in ten different positions by FIB-measurement. The results are $\bar{t}$ = 24 nm with SD = 3 nm, which fits the target value well. For the 40 nm Ag-reflectors, three different positions were measured with FIB, with the results being $\bar{t}$ = 67 nm with SD = 5 nm. This value differs a lot from the target value and is the same as the measured mean value from P-17 measurements.

The step height measurements for AlN/Ag/AlN-reflector stacks showed that, with the same sputter parameters as for pure Ag on glass, the mean values are almost the same as

the target values. Stacks of 20/40/20, 40/40/40 and 60/40/60 (all numbers are in nm) were fabricated and measured. For the 60/40/60 nm-stack, the measured mean step height is at 172 nm, which is the highest difference, being 12 nm, to the relating target value. The biggest range when depositing Ag directly on glass has been 30 nm. This shows that Ag-thin films expand differently on various substrate materials. One explanation might be the different surface energies of glass and AlN that lead to a diverse layer of growth of the Ag-thin films.

Regarding the FIB measurement of the 60/40/60-stack, the mean value distribution of the measured thicknesses are 69/49/84, since all three layers were visible, as can be seen in Figure 9.
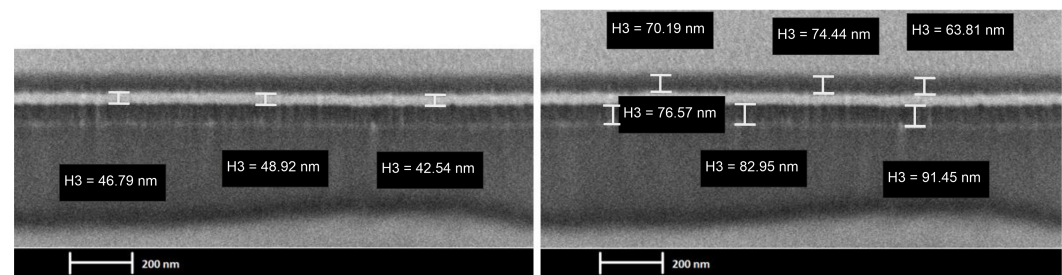

Figure 9. FIB measurement of the film thicknesses of a 60/40/60-reflector stack.

2.3. Summary

Table 3 provides an overview of most of the thin film depositions made, together with their film thickness evaluations. The target value t is the expected film thickness for each deposited layer, respectively, defined by the sputtering rate. Then, the measured $\bar{t}$ with its standard deviation SD and an evaluation on what would be the goal for further optimization steps in the future are given. For some of the fabricated thin films, it was not possible to evaluate the thicknesses reliably via FIB measurements. Each $\bar{t}$ represents the mean thickness of the reflectors deposited on one wafer. The SD of the Ag-reflectors after wet etching is relatively high due to the wet etching process or the accompanying lithography steps. As shown in Table 1, the Ag-thin films are uniform after deposition. Also, in the P-17 measurements of Ag-reflectors after lift-off, it is shown that better uniformity was achieved.

As shown in Section 2.1, the 20 nm Ag-thin films are not fully coherent. Thus, the measurements of the films thickness are adulterated and should be considered with caution.

3. Optical Characterization

All of the optical measurements were carried out by Bruker Vertex 70 FTIR with a wafer holder that ensures the orthogonal incidence of the measuring beam on the samples, as well as darkening fabric to eliminate disturbing ambient light. The aperture size which allows the measuring beam to pass through has been 0.5 mm for all FTIR measurements. Different sizes were tested and with smaller apertures, and the signal at the detector becomes too low; with bigger apertures, it becomes more difficult to align the beam on the reflectors. For the measurements in VIS, an Si-detector is used, with specification to detect the light down to a wavelength of 400 nm. However, below 450 nm, there will be noise with this FTIR, regardless of the measuring parameters. For gauging the transmittance, the beam of the FTIR passes through the sample and the transmitted light is detected for a certain interval of wavelength. Measuring the R is a bit more complex: a light redirecting mirror system has to be inserted in order to be able to measure the light reflected by the sample. This mirror system only allows for about 10×8 mm^2 fragments to be placed inside, so the wafer has to be diced in advance—unlike for the transmittance measurements.

3.1. Optical Characterization of Pure Ag-Reflectors

As part of preliminary investigations, and as presented in Figure 10, the optical characterization of pure Ag on glass showed that the measured reflectance reaches about 90% at $\lambda = 550$ nm for 40 nm (target value) Ag-thickness, which makes Ag a promising reflector

material for MEMS applications like the FPI in VIS. Also, in [12], it is shown that Ag exhibits the highest reflectance considering VIS as a whole compared to other metals like Al and Au.
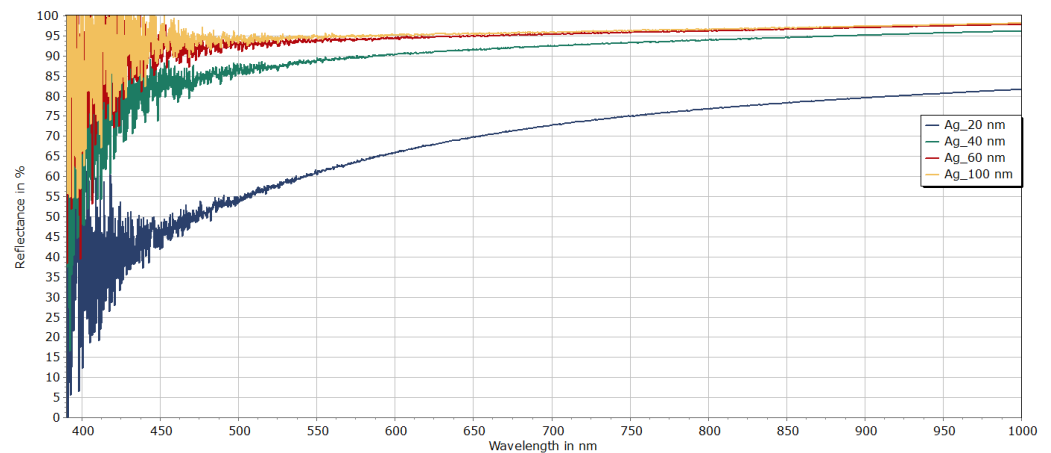

Figure 10. FTIR measured *R* of Ag-reflectors with different thicknesses in VIS and NIR.

In order to determine changes in optical properties over time, the transmittance *T* and reflectance *R* were measured over the course of two months. Whilst *T* has decreased by only 1%, namely from 23% to 22%, *R* had a more significant decrease of up to 5%, namely from 78% to 73%. This shows that some form of passivation of the Ag-thin films is needed.

The resulting absorption *A* (by $1 = T + R + A$) for 40–100 nm lies between 1 and 3%, which is lower than expected from the literature [12].

Ag is known for the effect of tarnish. It has one valence electron that can be donated. When the donated electron bonds with an acceptor, this process is referred to as oxidation. To prevent this oxidation from affecting the reflectors' optical properties, AlN should be used as passivation for the *MTF*. The characterization of pure Ag on glass can be considered as preliminary investigations to gain more knowledge about the behavior of Ag-thin films.

3.2. Characterization of AlN/Ag/AlN-Reflector Stacks in VIS

The goal is to characterize AlN/Ag/AlN-reflector stacks in VIS for use in optical applications such as FPI. Thus, *T* and *R* will be measured with the FTIR, while *A* will be derived from these two measurements. Note that, for measuring *R*, a reference mirror is needed, which is why a silver mirror with $R > 98\%$ above $\lambda = 500$ nm has been used for background measurement. AlN is used as a passivation material to prevent unwanted reactions on the surface of Ag that influences its optical properties. According to [20], AlN adheres very well to Ag, has suitable properties for optical applications [21] and can be integrated into the process flow relatively simply. N_2 does not cause any oxidation on Ag. It is also important to mention that AlN is free from absorption in VIS [22].

Whilst *T* and *R* can be adjusted through Ag thickness (as proven in Figure 10), they can also be varied by different AlN thicknesses for AlN/Ag/AlN-reflector stacks.

When increasing the thickness of Ag t_{Ag}, a higher *R* and lower *T* can be observed. This is one of the advantages of using *MTF* over DBR and defines the transmittance T_{FPI} of the device. However, when keeping the Ag layer at a constant thickness, T_{FPI} can be further customized by only changing t_{AlN}. As shown in Figure 11 *T* increases for a thicker AlN while *R* decreases for $\lambda \geq 600$ nm.
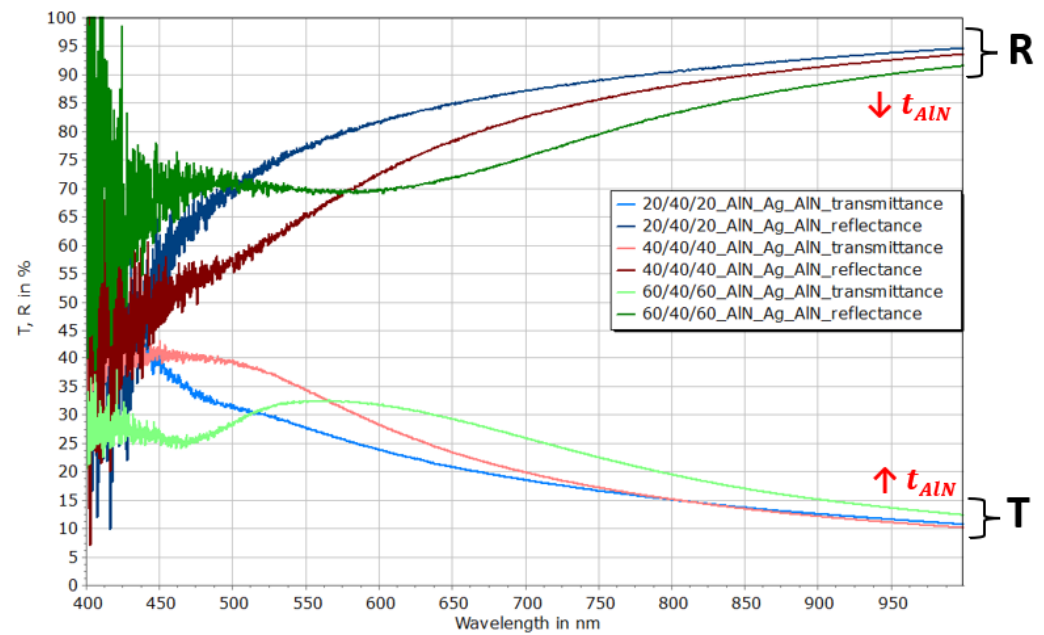
Figure 11. FTIR measured the *T* and *R* of the AlN-Ag-AlN-reflector stacks with different AlN thicknesses in VIS and NIR.

The resulting calculated absorption *A* from these measurements goes below zero. However, this result is based on the different measurements of *T* and *R*. And, because $A < 0$ is an improper value, the cause must lie in the measurement setup. There are multiple sources of error that could not be obliterated. As previously mentioned, a disturbing light has been eliminated. The angle of incidence is orthogonal for transmittance measurements. For measuring *R*, an additional mirror system is needed, which causes the angle of incidence to be at 11°. This angle cannot be adjusted because, otherwise, the measuring beam would no longer be focused on the sample. *T* has been measured with intentionally oblique angles of incidence at a wafer tilt of about 10°. While no difference in *T* has been recorded, this does not exclude a larger influence on the measurements of *R*. In addition to this, a reference mirror has to be used for the background measurement of the FTIR. A silver mirror with $R > 98\%$ above $\lambda = 500$ nm, according to the manufacturer information, was used. To compensate this deviation, the reflection curves were multiplied with a factor of 0.98. Still, its reflectance might have changed due to aging. Also, the FTIR measurements were carried out in a standard environment without any use of vacuum chamber. Particles in the air could have deflected the light. Upon using the reflector stacks shown here, it should be taken into consideration whether this problem can be reproduced and, if so, how it can be eliminated.

3.3. NIR

The AlN/Ag/AlN-reflector stacks fabricated in this work have not only been characterized in VIS, but also in the spectral range of NIR. For the FTIR measurements in NIR, the detector as well as the light source have to be adjusted. While a light source with visible light and a Si-detector are being used in VIS, they have to be swapped out for a near-infrared light source and an InGaAs-detector. The Quartz-VIS beam splitter remains the same for both types of measurements. This is in contrast to VIS AlN, which cannot be considered absorption-free in NIR [20]. As shown in Figure 12, the resulting absorption of the AlN/Ag/AlN-reflector stacks rises above 10% for the 60/40/60-stack. For the same Ag film thickness but thinner AlN, *A* becomes lower, which goes to show that some part of the absorption of these reflector stacks is also caused by the AlN.
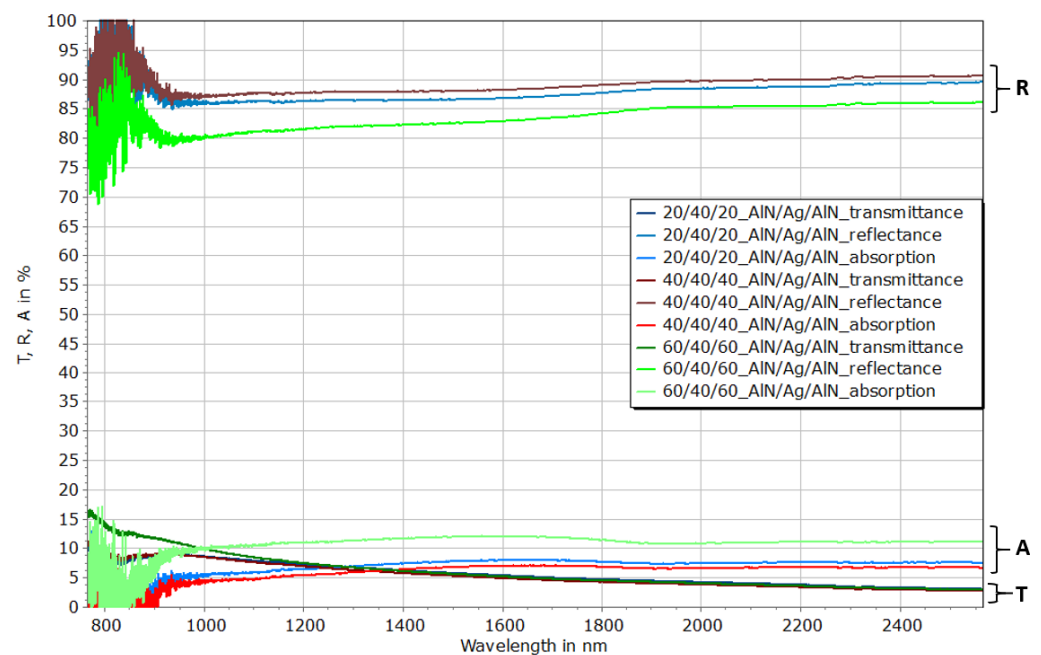
Figure 12. FTIR-measured *T* and *R* of AlN-Ag-AlN-reflector stacks with different AlN thicknesses in NIR.

3.4. Annealing

When integrated in any application, the thermal stability of the reflector stacks has to be considered as well because bonding will be necessary for fabricating FPI since the two opposing mirrors have to be brought together with a defined cavity inside. For the penetration of the light into the device, at least one side of the FPI has to consist of glass. Thus, anodic bonding is an obvious choice, which needs an increased temperature. By simulating the bond process, investigations on thermal stability can be made. Various bonding methods will be enabled in case the reflectors remain stable, for instance, parylene bonding, which can be performed at 300 °C as well. For this reason, some divided wafer parts were put into the process chamber of an SB6 from Süss at 400 °C, with N_2 supply and at normal pressure for 60 min. The heating time of 900 s and the cooling time of 2400 s down to 150 °C are added. Further cooling to 50 °C took an additional 30 min, which was realized by air cooling only. Under the microscope, some defects have been found on the annealed samples.

In Figure 13, the reflectors are imaged before the annealing with microscope-magnification of 20, which shows that no defects were present pre-annealing. Figure 14 shows the defects, that only appear after the annealing process, with a microscope magnification of 100. Because Ag and AlN have been sputtered in different sputter chambers (see Section 2), one explanation might be that some gas was trapped at the interface between the Ag and AlN, that extended due to the increased temperature and caused some cracks in those surfaces. Another possible reason would be that impurity atoms diffuse through the AlN-layer. The actual reason could not be clarified in this work. Since the reflector stacks were damaged after the annealing, the caused change in optical properties was examined. The differences in *T* did not exceed the measuring tolerances of the FTIR. As can be seen in Figure 15, a decrease in *R* of 2–4% was measured. For the 20/40/20-stack at $\lambda = 850$ nm, the biggest decrease was detected from *R* = 94% to *R* = 90%. Hence, the annealing has to be further investigated if one plans on fabricating FPIs with these reflectors, especially regarding the necessary bond process.

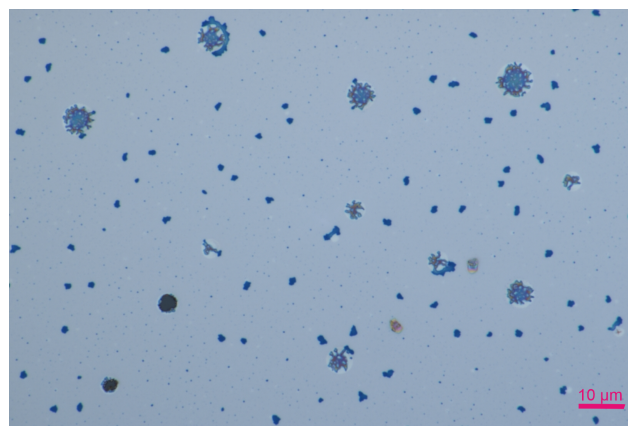**Figure 13.** Microscope image of a 60/40/60 nm reflector stack before annealing.

Figure 14. Detailed view on a 60/40/60 nm reflector stack after annealing.

4. Application of Fabricated Reflectors for FPI

Since the AlN/Ag/AlN-reflector stacks were fabricated with regard to usability in FPI application, a MatLab-simulation of T_{FPI} should show the quality of its behavior in VIS and NIR from λ = 400 nm to λ = 1000 nm. The basis of this simulation comes from the previously discussed FTIR measurements for T and R as well as the Airy equation [16]:

$$T_{FPI}(\lambda) = \frac{T^2}{(1-R)^2} \frac{1}{1 + \frac{4R}{(1-R)^2} sin^2\delta}. \tag{7}$$

Since the FTIR measurements were used as the basis for this simulation, the noise below 450 nm also stems from these measurements. With the specified parameters of $n = 1$ (air), the orthogonal incidence of light $\Theta = 0°$ and the optical phase difference $\Phi = 0°$, the spectral behavior was calculated.

Figure 16 qualitatively demonstrates the behavior of potentially fabricated FPI with mirrors of pairs of AlN/Ag/AlN-stacks of equal thickness for Ag, varying thickness of AlN, and an exemplary optical gap d of 2000 µm.

It is shown that T_{FPI} is adjustable by the adaptation of the thickness of AlN-layers only. Peaks in transmittance emerge at λ = 500 nm, λ = 572 nm, λ = 666 nm, and λ = 800 nm, respectively. The peaks are different in height for each t_{AlN}. Thus, the *FWHM* is customizable by varying t_{AlN}.
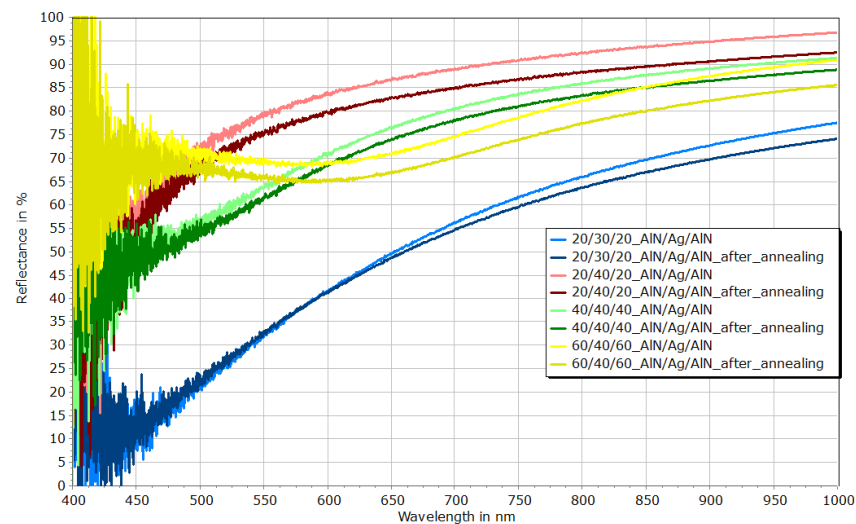
Figure 15. FTIR measured *R* of AlN/Ag/AlN-reflector stacks before and after annealing.
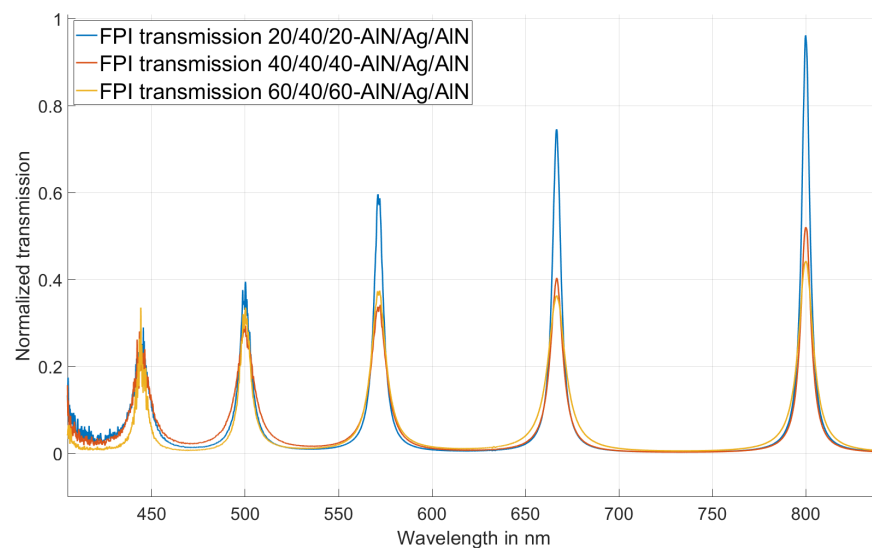

Figure 16. Simulated T_{FPI} with respect to different AlN thicknesses; airgap *d* = 2000 nm.

5. Conclusions

In this work, novel AlN/Ag/AlN-reflector stacks were fabricated and characterized with respect to FPI mirror application as a 150 mm wafer-level approach. First, the inline characterization was carried out to define the process parameters as well as a fabrication flow to generate reflectors with 2 mm in diameter. For preliminary investigations, Ag-reflectors were directly deposited on glass wafers to define a process flow, which showed that the lift-off is a suitable method to fabricate the mirrors. The *MTF* thickness was analyzed by measuring the step heights of both Ag-reflectors and AlN/Ag/AlN-reflector stacks with P-17, as well as the SEM analysis if possible. While pure Ag on glass was up to 30 nm thicker than expected, the AlN/Ag/AlN-stacks with the same sputter parameters as for the Ag, were close to the target values. Also, it was shown that the Ag-thin films form a homogeneous layer on glass, with $SD \leq 2\%$ on sheet resistance measured with the Polytec 280 SI. On SEM images, it could be determined that the Ag-thin films are coherent for 40 nm and larger thicknesses. In the optical analysis, transmittance and reflectance were measured for all fabricated reflectors. They are suitable for FPI application in VIS in terms of their high reflectance, which is higher than 90% at λ = 700 nm. Also, the resulting absorption, which previously held back *MTF* as opposed to DBR or SWG as mirrors, was very low in VIS, only rising up to about 10% in NIR. After an annealing process at 400 °C,

the reflectors were damaged which resulted in an overall decrease in *R* of about 2–4%. To give a final impression on the possible FPIs that could be fabricated from these reflectors, a MatLab simulation has shown the peaks in T_{FPI} as well as a customizable peak height and *FWHM* for different AlN thicknesses at a constant Ag thickness of 40 nm. In addition, the *MTF* reflectors showed very low stress after a P-17 (mechanical) stress measurement of 43 MPa for 40 nm Ag, which is an advantage to commonly used DBR as mirrors.

Overall, by examining the individual process steps with regard to process compatibility as well their characterization in VIS and NIR, the advantages of the newly fabricated AlN-Ag-AlN-reflector stacks have been shown, which opens a wide range of applications.

References

1. Crocombe, R.A. Portable Spectroscopy. *Appl. Spectrosc.* **2018**, *72*, 1701–1751. [CrossRef] [PubMed]
2. Martyniuk, M.; Silva, K.D.; Kala, H.; Zawierta, M.; Wallace, V.P.; Walus, K.; Faraone, L.; Shadrivov, I.V. Infrared and terahertz spectrally adaptive filters based on MEMS technologies. In Proceedings of the Smart Photonic and Optoelectronic Integrated Circuits 2023, San Francisco, CA, USA, 31 January–2 February 2023; He, S., Vivien, L., Eds.; International Society for Optics and Photonics, SPIE: Bellingham, WA, USA, 2023; Volume 12425, p. 124250H. [CrossRef]
3. Łabaj, F.; Kalwas, J.; Piramidowicz, R. Design and development of a miniature mid-infrared linear variable filter based spectrometer for environmental sensing. *Opt. Express* **2023**, *31*, 37583–37596. [CrossRef]
4. Yang, Z.; Albrow-Owen, T.; Cai, W.; Hasan, T. Miniaturization of optical spectrometers. *Science* **2021**, *371*, eabe0722. [CrossRef] [PubMed]
5. Liu, X.; Liu, W.; Ren, Z.; Ma, Y.; Dong, B.; Zhou, G.; Lee, C. Progress of optomechanical micro/nano sensors: A review. *Int. J. Optomechatron.* **2021**, *15*, 120–159. [CrossRef]
6. Helke, C.; Seiler, J.; Meinig, M.; Großmann, T.D.; Bonitz, J.; Haase, M.; Zimmermann, S.; Ebermann, M.; Kurth, S.; Reuter, D.; et al. Integration of (Poly-Si/Air)ⁿ Distributed Bragg Reflectors in a 150 mm Bulk Micromachined Wafer-Level MOEMS Fabrication Process. *IEEJ Trans. Electr. Electron. Eng.* 2023, *early view*. [CrossRef]
7. Blomberg, M.; Torkkeli, A.; Lehto, A.; Helenelund, C.; Viitasalo, M. Electrically tuneable micromachined fabry-perot interferometer in gas analysis. *Phys. Scr.* **1997**, *T69*, 119–121. [CrossRef]
8. Hakkel, K.D.; van Elst, D.M.; Petruzzella, M.; Ebermann, M.; Pagliano, F.; van Klinken, A.; Fiore, A. High-performance integrated mid-infrared filter arrays. *Electron. Lett.* **2022**, *58*, 884–886. [CrossRef]
9. Afandi, Y.; Parish, G.; Keating, A. Micromachined porous silicon Fabry-Pérot long wavelength infrared filters. *Sens. Actuators A Phys.* **2021**, *332*, 113101. [CrossRef]
10. Helke, C.; Hiller, K.; Seiler, J.; Erben, J.W.; Werner, T.; Reuter, D.; Meinig, M.; Kurth, S.; Otto, T. Nanostructured al SWG Reflectors on thin LP-Si3N4 Membranes as (TiO₂/SiO₂)³ Bragg Reflector Alternative for Vis Fabry-Pérot Interferometers. In Proceedings of the 2019 20th International Conference on Solid-State Sensors, Actuators and Microsystems and Eurosensors XXXIII (TRANSDUCERS and EUROSENSORS XXXIII), Berlin, Germany, 23–27 June 2019; pp. 1596–1599. [CrossRef]
11. Kerber, M.; Dick, B.; Fralick, M.; Jazo, H.; Waters, R. Design of highly reflective subwavelength diffraction gratings for use in a tunable spectrometer. In Proceedings of the SENSORS, 2009 IEEE, Christchurch, New Zealand, 25–28 October 2009; pp. 1984–1987. [CrossRef]
12. Bartek, M.; Correia, J.; Wolffenbuttel, R. Micromachined Fabry-Perot optical filters. In Proceedings of the ASDAM '98: Conference Proceedings—Second International Conference on Advanced Semiconductor Devices and Microsystems, Smolenice Castle, Slovakia, 5–7 October 1998; pp. 283–286. [CrossRef]
13. Hwang, C.S.H.; Lee, Y.; Ahn, M.S.; Chung, T.; Jeong, K.H. Visible range subtractive plasmonic color filter arrays using AG-AU alloyed nanoislands. In Proceedings of the 2018 IEEE Micro Electro Mechanical Systems (MEMS), Belfast, UK, 21–25 January 2018; pp. 535–538. [CrossRef]

14. Cao, P.; Huang, W.; Guo, H.; Zhang, Y. Performance of a Vertical 4H-SiC Photoconductive Switch with AZO Transparent Conductive Window and Silver Mirror Reflector. *IEEE Trans. Electron Devices* **2018**, *65*, 2047–2051. [CrossRef]

15. Alyousef, H.A.; Hassan, A.; Zakaly, H.M.H. Reactive magnetron sputtered AlN thin films: Structural, linear and nonlinear optical characteristics. *J. Mater. Sci. Mater. Electron.* **2023**, *34*, 1088. [CrossRef]

16. Macleod, H.A. *Thin-Film Optical Filters*, 4th ed.; CRC Press: Boca Raton, FL, USA, 2010.

17. Fornari, C.; Fornari, G.; Rappl, P.; Abramof, E.; Travelho, J. Monte Carlo Simulation of Epitaxial Growth. In *Epitaxy*; BoD—Books on Demand: Norderstedt, Germany, 2018.

18. Tencor® FLX-2320. *Thin Film Stress Measurement, User Manual*; KLA Corporation: Milpitas, CA, USA, 1994.

19. Schmidt, B. Eigenspannungen in düNnen Schichten. 2016. Available online: https://docplayer.org/21132374-Eigenspannungen-in-duennen-schichten.html (accessed on 28 November 2022).

20. Krujatz, J. Herstellung von Spiegelschichtsystemen auf der Basis von Aluminium oder Silber für den Einsatz in der Mikrosystemtechnik. Ph.D. Thesis, Chemnitz University of Technology (TU Chemnitz), Zentrum, Germany, 2002.

21. Meinel, K.; Melzer, M.; Stoeckel, C.; Shaporin, A.; Forke, R.; Zimmermann, S.; Hiller, K.; Otto, T.; Kuhn, H. 2D Scanning Micromirror with Large Scan Angle and Monolithically Integrated Angle Sensors Based on Piezoelectric Thin Film Aluminum Nitride. *Sensors* **2020**, *20*, 6599. [CrossRef] [PubMed]

22. Adachi, S. *Optical Constants of Crystalline and Amorphous Semiconductors: Numerical Data and Graphical Information*; Springer: Boston, MA, USA, 1999.